

Article

Design and performance of a novel tapered wing tiltrotor UAV for hover and cruise missions

E.U. Rojo-Rodriguez ^{1,†} , E.G Rojo-Rodriguez ^{1,†} , S. Araujo-Estrada ^{2,†}  and O. Garcia-Salazar ^{1,†*} 

¹ Aerospace Engineering Research and Innovation Center, Faculty of Mechanical and Electrical Engineering, Autonomous University of Nuevo Leon, Apodaca NL, Mexico; edgar.rojordrg@uanl.edu.mx; erojor@uanl.edu.mx; octavio.garciasl@uanl.edu.mx

² Department of Aeronautical and Astronautical Engineering, University of Southampton, Southampton SO16 7PX, U.K.; s.araujo-estrada@soton.ac.uk

* Correspondence: octavio.garciasl@uanl.edu.mx

† These authors contributed equally to this work.

Version September 9, 2024 submitted to *Machines*

Abstract: This research focuses on a novel convertible unmanned aerial vehicle (CUAV) featuring four rotors with tilting capabilities combined with tapered form. The research studies the transition motion between multi-rotor and fixed-wing modes based on the mechanical and aerodynamics design as well as the control strategy. The proposed CUAV involves information about design, manufacturing, operation, modeling, control strategy, and real-time experiments. The CUAV design considers a fixed-wing with tiltrotors and provides the maneuverability to perform take-off, hover flight, cruise flight, and landing, having the characteristics of a helicopter in hover flight and an aircraft in horizontal flight. The manufacturing is based on additive manufacturing, which facilitates the creation of a lattice structure within the wing. The modeling is obtained using the Newton-Euler equations, and the control strategy is a PID controller based on a geometric approach on SE(3). Finally, The real-time experiments validate the proposed design for the complete regime of flight, and the research meticulously evaluates the feasibility of the prototype and its potential to significantly enhance the mission versatility.

Keywords: Convertible UAV; Tilting rotors; Manufacturing; Design; Real-time experiments

1. Introduction

In recent years, Unmanned Aerial Vehicles (UAVs) have become increasingly common in several civilian and military applications, among them, it is mentioned search and rescue, highway patrol, and inspecting infrastructure such as power lines, bridges, factories, buildings, exteriors, sewers, railroads, and wind turbines. There exist three main types of UAVs: multirotors, airplanes, and convertible UAVs (non-conventional configurations), [1].

The take-off and landing have historically presented difficulties for UAVs since these have been a problem because of the limitations involved in each different configuration. In this sense, a fixed-wing UAV presents high aerodynamic performance and requires a runway in order to take off and land; however, a rotary-wing UAV suffers performance limitations in terms of endurance, range, and maximum forward speed. In order to combine these capabilities of the fixed-wing and rotary-wing UAVs, a solution is proposed in this paper as tiltrotor configuration with a tapered wing.

Classic fixed-wing vehicles require dedicated runway infrastructure, limiting their operational reach [2]. Convertible aircrafts, on the other hand, can operate from confined spaces and eliminate the need for extensive runways. This translates to increased accessibility for remote locations,

30 urban environments, and disaster zones where traditional landing strips might be unavailable or
31 damaged [3]. While offering vertical agility similar to helicopters, convertible vehicles can transition to
32 fixed-wing flight for extended range and higher cruise speeds compared to rotary-wing vehicles. This
33 provides a significant advantage in terms of operational efficiency, particularly for applications such as
34 long-distance cargo delivery, search and rescue missions over vast areas, or border patrol activities [4].

35 Research on convertible UAVs requires knowledge of rotary-wing and fixed-wing vehicles to
36 combine hover and cruise flight properties; it means a CUAV that performs a complete flight: take-off,
37 hover, cruise, and landing modes. Some convertible UAVs can be found in [5], computational fluid
38 dynamics (CFD) simulation and aerodynamic characterization in [6], flight dynamics modeling and
39 stabilization in [7], and additionally, the tilting mechanism was designed in [8]. The development
40 of convertible vehicles, tilt-rotor UAVs, tilt-wing UAVs, tail-body or tailsitter UAVs, has garnered
41 significant interest in the scientific community [9], [10], [11]. The domain of convertible UAV
42 indexing presents a multifaceted landscape. While a multitude of researchers have opted for bespoke
43 designs with unique implementation strategies, this very diversity creates a significant challenge for
44 comprehensive study. Nonetheless, several prominent approaches hold particular significance and
45 warrant mention within the relevant literature. These approaches include: A tilt-rotor convertible UAV
46 involves a quad-rotor design equipped with a tilting mechanism, as addressed in [12]. This mechanism
47 provides the ability to dynamically change the direction of propulsion. This vehicle was stabilized with
48 a nonlinear control for the complete regime of flight, and the autopilot was developed using a low-cost
49 DSP embedded system to achieve real-time experiments. A prototype employing vectorized thrust
50 was presented in [13], enabling the capability for motion without the need for corresponding body
51 movement. This algorithm was validated in real-time experiments, showing the effectiveness of the
52 proposed controller. In [14], the development of the transitioning vehicle called Cyclone was proposed,
53 whose mission is to perform hover and horizontal flights considering a control with incremental
54 nonlinear dynamic inversion. The real tests demonstrated the vertical take-off and landing capabilities
55 of the vehicle. Furthermore, research on lightweight materials is crucial to optimize performance and
56 range [15] [16]. These advancements can have a ripple effect, benefiting the development of future
57 generations of both conventional and unconventional aircraft.

58 In [17], a flight control system of a small tiltrotor UAV was proposed, and it is based on an
59 improved mathematical model. The proposed controller is based on an eigenstructure assignment, and
60 the proposed approach has been validated in a wind tunnel test and real-time flights. In [18], authors
61 presented a methodology to design a tiltrotor micro air vehicle in order to perform hovering and
62 cruise flight scenarios. Results showed the aerodynamic parameters of the proposed vehicle. Authors
63 in [19] proposed a geometrically compatible integrated design to develop for the conformal rotor
64 and nacelle of the distributed propulsion tilt-wing UAV. This methodology considered the complex
65 geometric constraints and coordinated the aerodynamic efficiency of the rotor and nacelle, allowing
66 a low drag. A tiltrotor UAV was presented in [20] whose configuration drives the attitude based on
67 rotors tilting. The control strategy is based on a bounded smooth function, and it was implemented
68 in real-time flights. In [21], a small trirotor test bed with tilting propellers was proposed to validate
69 the flight control laws. The controller algorithm is based on a nonlinear dynamic inversion with
70 two layers. The lower layer involves attitude stabilization, while the higher layer manages trajectory
71 tracking. Authors in [22] worked on a robust adaptive mixing controller to achieve trajectory tracking
72 of a quad-tiltrotor convertible plane, and the mathematical model is obtained using Euler-Lagrange
73 formalism. To validate the controller, authors executed hardware-in-the-loop experiments. In [23],
74 a model predictive controller was proposed for tiltrotor UAVs demonstrating the performance in
75 real-time flights. The controller strategy considered a control allocation algorithm, and the model
76 predictive control constitutes a unified nonlinear control for the convertible UAV that performs the
77 complete flight. In [24], authors presented a CFD (computational fluid dynamics) simulation for a
78 tiltrotor UAV in order to examine the flow fields on the fuselage and rotor under the transition mode
79 of the vehicle. A transition strategy design based on optimization methods as proposed in [25], the

80 transition problem is solved using the optimal method with nonlinear programming. The optimization
81 results showed that the transition strategy can manage the relationship between transition time, control
82 input, and attitude stability. The work in [26] proposed a multi-disciplinary optimization algorithm
83 for preliminary convertible UAV design. This design is based on aerodynamic models, and it is
84 validated using optimization techniques. [27] presented the design of a convertible UAV considering
85 the parameters of the rotor, propeller, wing, and airfoil selection. The CUAV design was based on
86 a flying wing and modified to add the tilting rotors. A basic PID controller was tested in real-time.
87 In [28], authors focus on a controller based on an MPC-based Position for a tiltrotor tricopter VTOL
88 UAV. The controller involves a conventional control in the outer loop, while the inner loop is an MPC
89 controller. The simulation was executed for trajectory tracking under the realistic actuator limits.
90 However, our proposed vehicle differs from those published in the literature since it involves tiltrotor
91 mechanisms combined with a tapered wing, which, in hover flight, the vehicle is controlled via the
92 propulsion system providing vertical lifting acting against the gravity field. In horizontal mode, the
93 convertible vehicle is airborne, so that the outer body surface (tapered wing) provides the lift force to
94 maintain the horizontal flight.

95 The main contribution of this paper is a novel convertible tiltrotor UAV using a tapered wing in
96 order to perform a hover flight as a helicopter and a horizontal flight as an airplane. The methodological
97 process is outlined to achieve a comprehensive design to address the convertible configuration, as well
98 as the interaction between manufacturing and flight computer development. Real-time experiments
99 are performed to validate system behaviors. The contribution of this paper is summarized as follows:

- 100 1. Development of a novel tapered wing tiltrotor UAV for hover and cruise missions.
- 101 2. A scheme of guidance, navigation, and control based on the special Euclidean group $SE(3)$ for
102 the convertible UAV is proposed.
- 103 3. The proposed convertible UAV is tested to obtain the performance in real-time flights.

104 The rest of this paper is organized as follows: section 2 presents information about the UAV
105 configuration, operational functions, performance, and manufacturing. Section 3 describes the
106 equations of motion for the convertible UAV using the Newton-Euler formulation and proposes
107 the geometric navigation based on the special Euclidean group $SE(3)$, with a guidance frame and a
108 saturated PID control. Section 4 presents the experimental platform and the autonomous navigation
109 results of the convertible UAV. Finally, conclusions are given in section 5.

110 2. Design proposal

111 This section outlines a comprehensive design proposal for a convertible Unmanned Aerial Vehicle
112 (UAV) aimed at addressing the flight mission for both hover flight and cruise flight. Our proposal
113 is motivated by the ever-increasing demand for versatile UAV systems capable of dynamically
114 adapting to diverse and complex mission requirements. The subsequent sections address the
115 configuration, actuation, manufacturing, and performance, elucidating the challenges encountered in
116 the development and deployment and presenting significant potential for expanding the capabilities
117 of UAVs. Figure 1 shows the schematic of the proposed convertible UAV and the operation efficiently
118 under various flight conditions.

119 2.1. UAV configuration

120 The proposed UAV configuration plays a pivotal role in its adaptability and flight capabilities.
121 The main feature of this configuration is the use of frontal rotors with tilting capabilities and the rear
122 rotor with a coaxial mechanism providing sufficient lift in the hover flight while the wing is a T-shaped
123 design providing the lift force in the forward flight.

124 The frontal tiltrotors enable the UAV to transition seamlessly and continuously between hover
125 and cruise modes, as shown in Figure 2. During take-off and hover, the rotors are oriented vertically,
126 providing the necessary lift and control (right side of Figure 2). As the UAV transitions to forward



Figure 1. UAV mission proposal over different areas.

127 flight, the rotors tilt horizontally, allowing the fixed-wing to generate lift in relation to airspeed (left
 128 side of Figure 2). This dynamic configuration offers the best of both modes, combining the agility and
 129 versatility of a multirotor with the efficiency and endurance of a fixed-wing aircraft.

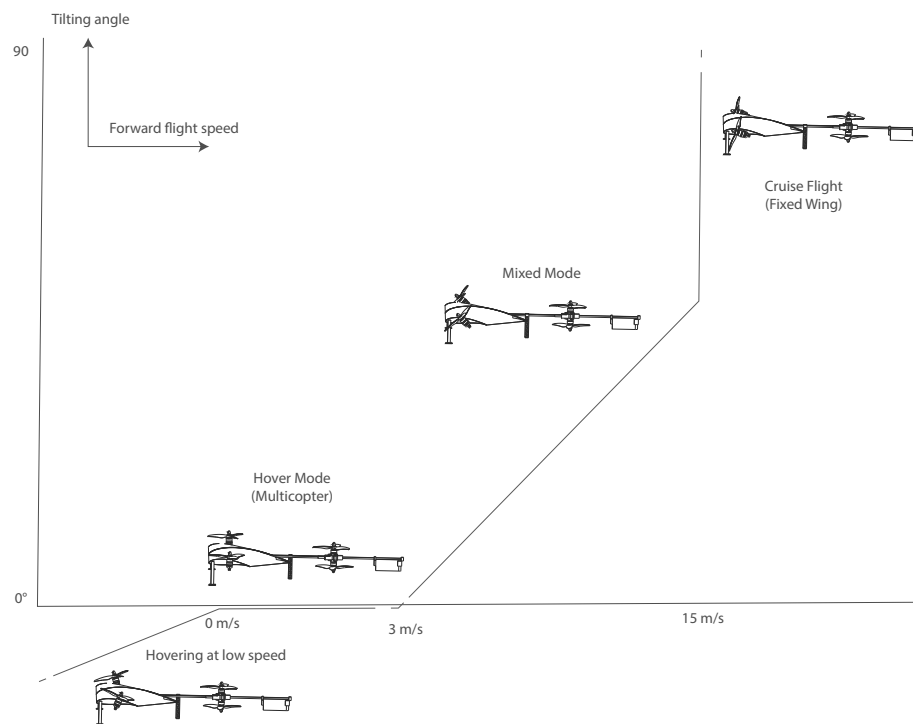


Figure 2. Flight phases for convertible UAV.

130 The T-shaped distribution of the frontal rotors ensures stability and control during the transition
 131 phase and fixed-wing flight. This configuration optimizes the UAV aerodynamic properties and
 132 reduces drag, improving performance and energy efficiency. Following this convention, the proposed
 133 configuration, as shown in Figure 3, involves the entire array of propulsion and structural fuselage.

134 2.2. Physical parameters

135 This section presents the physical parameters of the platform, detailing its components in both
 136 configurations and highlighting the mechanisms that enable its convertibility. In the context of this

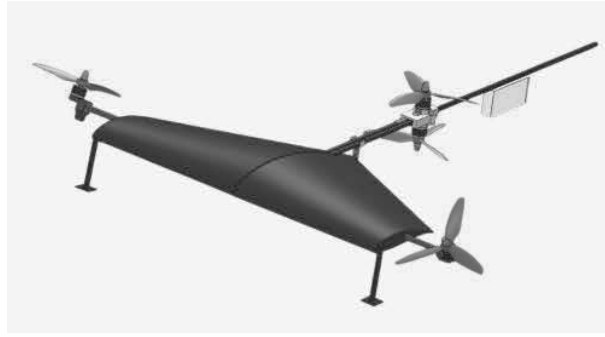


Figure 3. Proposal of the convertible UAV.

137 convertible UAV design, a total weight estimation is required to reach the hover mode and to facilitate
 138 the analysis of the dual operational configuration. The first stage involves a multirotor configuration
 139 that supports the vehicle weight and enables flight control. However, the design also necessitates a
 140 fixed-wing configuration for forward flight. Consequently, appropriate airfoil selection and subsequent
 141 lift generation estimation are crucial considerations. It is important to note that the design is constrained
 142 by a maximum volume, with a boundary box of 0.065m × 0.070m × 0.020m, to maintain a micro UAV
 143 classification [29]. The proposed parameters are detailed next:

Parameter	Value
Span	0.04m
Wing Root	0.024m
Wing Tip	0.012m
Wing Surface	0.075m ²
Frontal Arms length	0.025m
C.G. to frontal	0.018m
C.G. to bottom	0.016m
Airfoil	FX-63
Incidence angle	3 °
Weight	420gr

Table 1. Aircraft physical parameters

144 These design parameters are chosen with the main objective of minimizing weight and enabling
 145 the complete regime of flight. Consequently, a total weight of less than 500 grams and a compact
 146 volume are prioritized. These parameters significantly contribute to an aircraft maneuverability within
 147 a confined environment. Additionally, the wing surface selection process considers the airfoil type and
 148 its capacity to generate sufficient lift for sustained forward flight.

149 Note that equation $n = (L + F_T)/(W)$ presents the relationship between Lift force, rotor force,
 150 and weight; a factor must be equal to or greater than 1 for the aircraft to fly. Considering load factors,
 151 this convertible UAV requires to be designed for two flight regimes. In multirotor mode, the aircraft
 152 is prepared for 4g to handle the fast maneuvers needed for stability and precision. However, for
 153 fixed-wing mode, the design needs to consider the different load factors experienced during cruise
 154 flight. This presents a design challenge for the convertible UAV. The structure needs to be robust
 155 enough to withstand 4g accelerations in multirotor mode while also being lightweight for efficient
 156 fixed-wing flight. Additionally, the wing design, selected tapered form, of the convertible UAV
 157 is optimized for both high lift generation during multirotor operation and efficient aerodynamic
 158 performance during fixed-wing flight.

159 This design is developed based on additive manufacturing (AM) techniques to find lightweight
 160 parameters and integrate the entire mechanism into the internal structure. Different materials are
 161 used for various groups of parts, considering structural and impact reasons, [16], as determined
 162 from structural optimization. The system is evaluated under static conditions, as this study focuses

Part	Material
Wing Surface	ABS
Structural Frontal Arm (Left and Right)	Fiber Glass tube
Rotor Adapter	PETG
Tilt mechanism	HIPS

Table 2. Materials Specifications

163 on representing maximum structural stress in dynamic environments. It uses maximum thrust for
 164 information on internal structure, which informs optimization and deflection rejection. It is performed
 165 multiple studies to develop and validate the effectiveness of geometrical optimization of this model,
 166 which is based on AM and also uses Solid Isotropic Material with Penalization (SIMP). SIMP is
 167 a powerful optimization algorithm determining the optimal material distribution within a design
 168 domain. SIMP generates lightweight structures with enhanced stiffness and strength by iteratively
 169 removing material from low-stress regions. When it is combined with 3D printing, this approach
 170 enables the fabrication of complex, lattice-like structures that would be infeasible using traditional
 171 manufacturing methods,[30]. To effectively utilize SIMP optimization, it is essential to couple it with
 172 finite element method (FEA) and computational fluid dynamics (CFD) simulations. FEA provides
 173 accurate predictions of structural behavior under various loading conditions, while CFD enables
 174 aerodynamic performance evaluation. By iterative refining the design based on simulation results,
 175 engineers can achieve optimal component performance.

176 A maximum input force for thrust force is applied on each rotor base, also represented in Figure 5
 177 representing the maximum maneuver allowed by this type of aircraft. The center of gravity is selected
 178 as a fixed point for statics study, similar to a ground experiment on deformation effects 6, allowing for a
 179 geometrical profile of deformation, as depicted in Figure 6 and 8 evaluating both effects on convertible
 180 aircraft. Iterations show a maximum deformation of 0.9258mm on noncritical parts at hover phase
 181 6 and 0.2921mm for cruise phase 8, results expected due to different forces distribution 5 7, which is
 182 expected on lightweight structures. In this specific case, it is concentrated over the bottom part, which
 183 is only affected in hover mode and compensated by the control scheme.

184 The primary objective of this analysis is to evaluate the deformation characteristics and verify the
 185 structural integrity of the model under specified loading conditions. By utilizing ANSYS Mechanical,
 186 the objective is to identify potential weaknesses and ensure that the structure can withstand the applied
 forces without compromising its integrity.

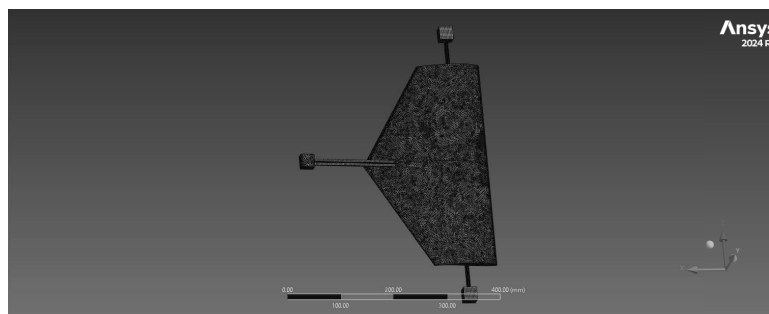


Figure 4. FEM mesh definition.

187 The model created for this study is reduced to a mechanical representation of aircraft in order
 188 to simplify the model and develop a mesh of 2.5mm of element size with a level of 7 at adaptive
 189 sizing resolution. These mesh elements were selected due to the minimum element size on the system
 190 with a 4.01mm element, which is covered by the 1.25mm change on elements selected on configurations.
 191

192

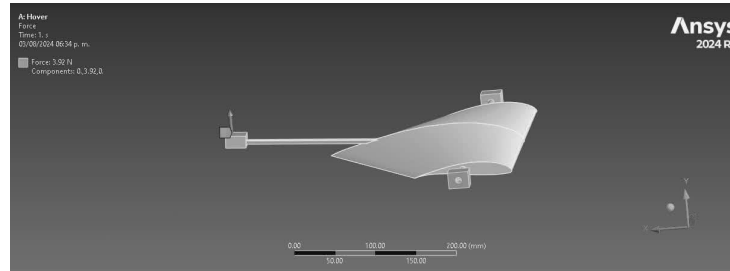


Figure 5. Forces definition for hover case.

193 For hover conditions, forces are placed at rotor points due to its nature of multi-rotor, red zones at
 194 figure 5, selected for this study as maximum force developed by rotor configuration of 3.92N for each
 195 rotor.

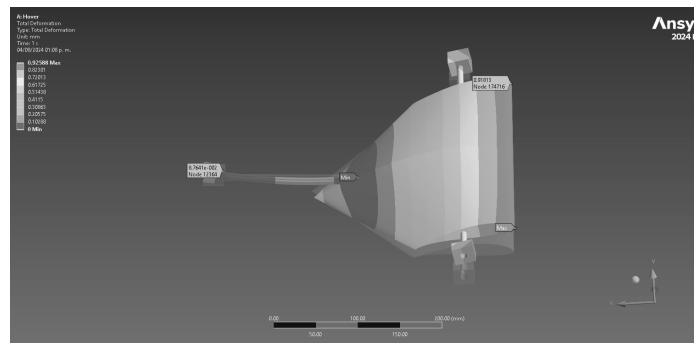


Figure 6. Structure deformation for hover condition.

196 Considering that the main structure is developed by ABS material and distributed to rotors by
 197 fiberglass tubes, it takes account of wing deformation, as shown in Figure 6,. It has a probe illustrating
 198 the maximum deformation point at the inlet part. This behavior is ideal for this configuration due to
 199 the type of manufacture, which demonstrates the effectiveness of SIMP optimization, placing forces at
 200 required points. For this geometry, it is used to place internal structures on those points.

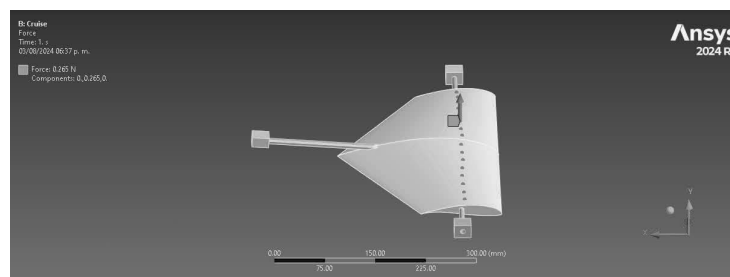


Figure 7. Forces definition for cruise case.

201 It is considered the cruise flight part of the study to verify wing effectiveness; in this case, it is
 202 developed as a force on 1/4 part of the wing, which is later demonstrated in the CFD study. Addressing
 203 that point are selected a distribution of forces points at the wing surface as seen in Figure 7, which are
 204 a distribution of the 14m/s case, becoming a Gaussian distribution due to this wing geometry, with a
 205 total force of 4.24N, consider as a force for cruise flight which is the required to lift the whole aircraft.

206 Actual results show 0.29098mm as the maximum point of deformation, which is ideal for this
 207 case of micro UAV, making a structure that could handle the system and 0.17714mm on rotors pads,
 208 considering that this deformation would not affect the final rotor force vector.

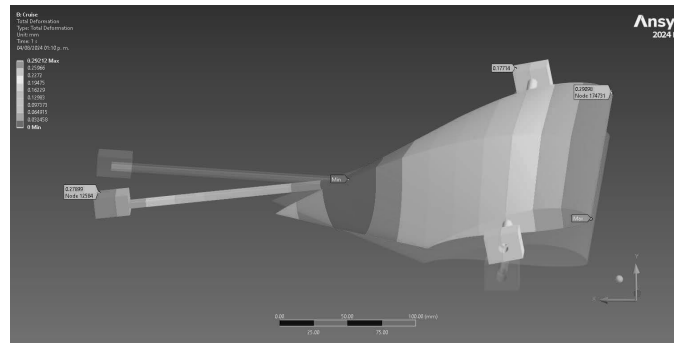


Figure 8. Structure deformation for cruise condition.

209 Considering the concentration of deformation shown in Figure 6, it is evident that the frontal
210 rotors would experience the most deformation and equivalent stress, making it a critical point for
211 examination. The frontal arms exhibit a maximum deformation of 0.92mm under extreme conditions,
212 although such conditions may not occur in real-world scenarios. However, given that these are made
213 of a polymeric material of ABS nature, these can withstand this deformation while maintaining proper
214 operation.

215 It is important to note that this structure is designed to withstand and exceed forces generated by
216 aerodynamic conditions and rotor forces. This decision ensures the ability to accommodate dynamic
217 behaviors without encountering issues. The accuracy and reliability of CFD simulations heavily
218 depend on the mesh quality used to discretize the computational domain. This study highlights the
219 significance of mesh refinement in capturing the intricate aerodynamic features of a wing. For this case,
220 an adaptive mesh is selected. The outer air domain, which extends 150 mm from the wing, is crucial
221 for capturing the far-field effects of the airflow, as shown in figure 9. A coarser mesh is sufficient in
222 this region to reduce computational cost while accurately predicting the overall flow behavior. Closer
223 to the wing, within a 500 mm proximity, the mesh is refined to capture the near-field aerodynamic
224 effects more accurately, using a body influence, which affects 10mm element size modification. The
225 wing surface requires a highly refined mesh to capture the boundary layer effects and surface pressure
226 distribution accurately. An element size of 1 mm is employed over the wing surface, essential for
227 resolving the fine details of the flow around the wing, including the leading and trailing edges. To
228 capture accurately the boundary layer development, 10 inflation layers are used on the wing surface,
229 validated in figure 10. These layers allow for a gradual transition from the wing surface to the
230 free-stream, ensuring that the viscous effects are well-resolved. The first layer thickness is carefully
231 chosen to capture the near-wall gradients accurately.

232
233 The system is analyzed under various scenarios, particularly at an airspeed of 14m/s, as shown
234 in Figure 11. It is observed that the system interacts with the air during cruise flights in a similar way
235 to a flying wing, thanks to the proposed design. This design minimizes external parts, exposing only
236 the rotors and fixed wing, thus optimizing aerodynamic efficiency.

237 The CFD analysis employed a high-fidelity model encompassing both the wing and rotor
238 geometries. The simulations are run with an inlet velocity of 14 m/s, representing typical cruise
239 conditions. The selection of the FX63 airfoil for the wing is based on its well-documented performance
240 characteristics.

241
242 Figure 11 presents contoured colored by velocity magnitude, visualizing the flow behavior
243 around the wing. The absence of significant deviations or swirling patterns in the contour suggests a
244 predominantly laminar (non-turbulent) flow regime under the simulated conditions.

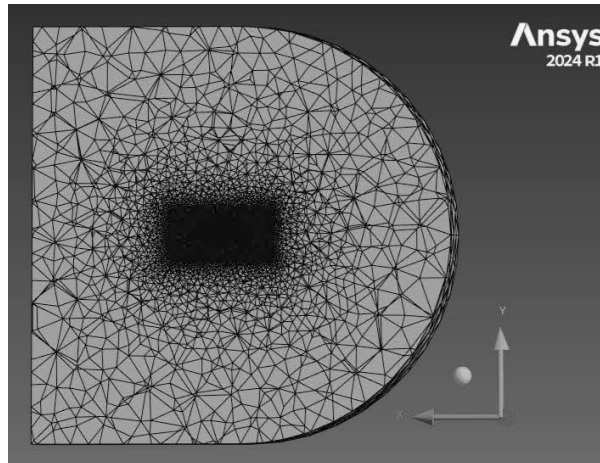


Figure 9. General CFD Mesh.

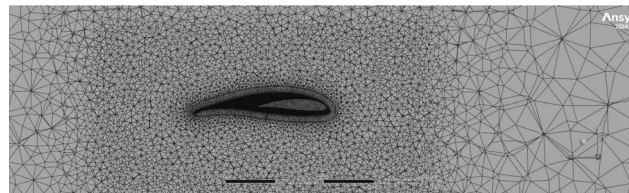


Figure 10. Detailed CFD Mesh with the airfoil.

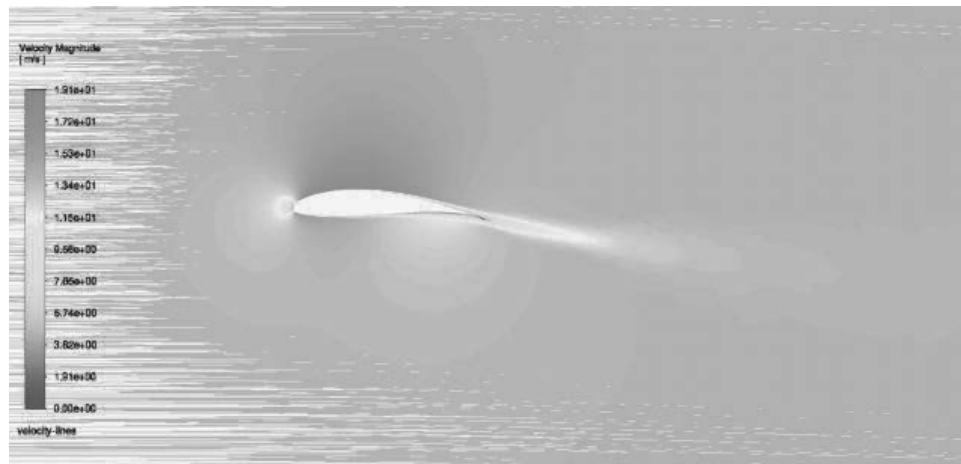


Figure 11. Airflow distribution.

245 Furthermore, the analysis reveals that the airfoil design effectively accelerates the incoming flow.
246 The velocity magnitude increases from the initial 14 m/s at the inlet to approximately 36 m/s over the
247 wing surface. This acceleration is crucial for generating lift, a vital force for flight.

248 Understanding pressure gradients is vital for identifying regions of flow separation and potential
249 stall. This information is crucial for designing airfoils that maintain smooth airflow, enhancing the
250 UAV's performance and stability; for that reason, it is analyzed in figure 12. Pressure distribution
251 data is essential for structural analysis. It helps determine the aerodynamic loads acting on the airfoil,
252 which is necessary for ensuring the structural integrity and durability of the UAV. The CFD results
253 reveal detailed pressure contours and distributions over the FX63-137 airfoil. High-pressure regions on
254 the lower surface and low-pressure regions on the upper surface indicate the generation of lift. Areas

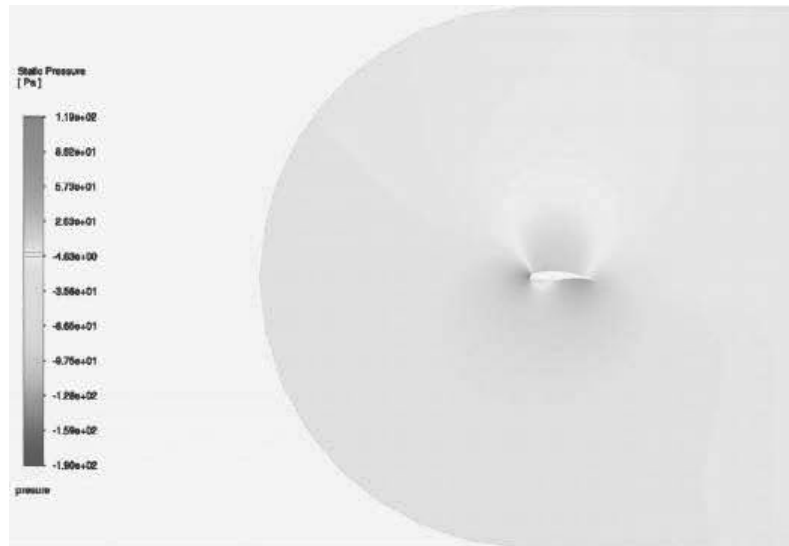


Figure 12. Pressure distribution at cruise flight.

of adverse pressure gradients highlight potential regions for flow separation, providing insights into the airfoil's stall characteristics.

Multiple CFD studies were performed, and more prominent results are presented in table 3, which mention different scenarios of this aircraft. The ideal scenario for this design is design point (DP) 9, where the aircraft flight is stable at the cruise case, considering that 3° is the incidence angle developed for this design.

Design Point	Angle of Attack	Airspeed (m/s)	Lift (N)	Drag (N)
DP 0	0	10	1.4831801	0.18688435
DP 1	0	5	0.33591906	0.049558448
DP 2	0	14	3.0199035	0.35773087
DP 3	0	20	6.3607885	0.71587954
DP 4	1	10	1.7161523	0.21013449
DP 5	2	10	1.9474965	0.23701694
DP 6	3	10	2.1824285	0.26784294
DP 7	10	10	3.8275471	0.59171158
DP 8	15	10	4.9289569	0.9282643
DP 9	3	14	4.3934829	0.52030514
DP 10	20	14	8.181392	2.3159387
DP 11	30	14	8.2654707	4.2134698
DP 12	45	14	7.5462137	7.0732765
DP 13	-10	14	-1.1898977	0.73946404

Table 3. CFD Results

Other cases are also analyzed as high angles of DP 10-13, showing that this aircraft could improve forces using more prominent cases, but with a drag consequence, which let us make future considerations for aggressive maneuvers.

2.3. UAV actuation

With rapid technological advancements, integrating complex actuation systems has revolutionized the efficacy and versatility of unmanned aerial vehicles (UAVs) across various mission profiles. One of the main advantages of UAV actuation lies in its ability to augment mission adaptability and responsiveness [31]. By incorporating dynamic actuation mechanisms, such as articulated wings,

269 tilting rotors, or swiveling thrusters, UAVs can swiftly adapt to diverse environmental conditions
270 and operational requirements. This agility enables UAVs to navigate challenging terrains, circumvent
271 obstacles, and execute precision maneuvers with unparalleled efficiency.

272 The core of our convertible UAV design lies the innovative configuration of frontal rotors featuring
273 tilting capabilities. These rotors are actuated by precision servomotors, enabling dynamic adjustments
274 to their orientation. This pivotal feature facilitates the seamless transition between vertical take-off
275 and landing (VTOL) operations and cruise flight, enhancing the versatility of the UAV.

276 For our prototype, a tilting mechanism based on gear transmission of servomotor force is
277 developed. This mechanism directly controls the tilting angle, as depicted in Figure 13. Note that the
278 tilting rotors are independent, allowing the system to be used as a differential one. V-22 aircraft were
279 used as inspiration for rotor placement due to their performance and wing-rotor interaction, allowing
280 better maneuverability.

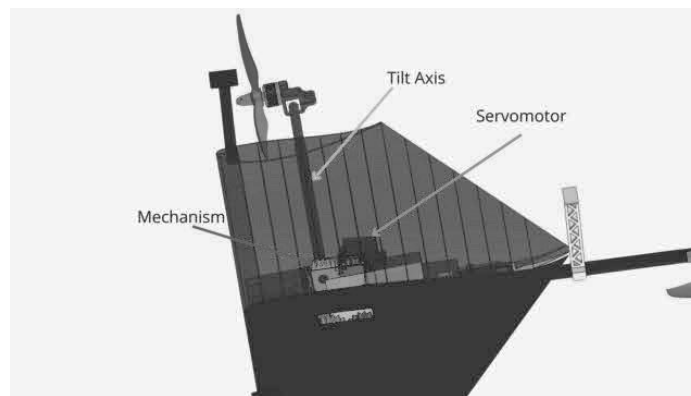


Figure 13. Tilting Mechanism for rotor direction.

281 2.3.1. Hover flight

282 Vertical Take-Off and Landing (VTOL) operations are crucial for unmanned aerial vehicles (UAVs),
283 especially in scenarios where confined spaces or quick deployment are imperative. For our proposed
284 vehicle in hover mode, the frontal rotors are strategically positioned vertically to generate the necessary
285 lift and directional control, facilitating stable take-off, landing, and low-speed flight maneuvers. These
286 rotors have precision movement capabilities, enabling orientation adjustments through tilting actions
287 without the need for rotor speed variation. This innovative approach ensures efficiency and establishes
288 a robust motion for hover mode control.

289 Furthermore, the differential control system governing the frontal rotors amplifies the CUAV
290 agility and precision across both hover and cruise flight phases. By independently adjusting the
291 tilt angles of each rotor, the CUAV gains precise control over pitch and yaw, facilitating seamless
292 transitions between flight modes and empowering the vehicle to execute complex maneuvers with
293 ease. This level of control versatility enhances operational fluidity and renders the CUAV adaptable
294 to diverse mission requirements and environmental conditions. This condition stipulates that only
295 saturated angles are applied to small motion, primarily utilizing the tilting mechanism for yaw motion
296 while ensuring stability. The roll motion is obtained by the differential velocity of rotor 1 and rotor 2,
297 and the pitch motion is obtained through the differential coupled rotors 1-2 and the coaxial rotors 3
298 and 4. The yaw motion is achieved by differential tilting rotors for 1 and 2; see Figure 14.

299 2.3.2. Cruise flight

300 Once the UAV is airborne and ready to transition to cruise flight, the servomotors engage,
301 facilitating the seamless transition of the rotors from vertical to horizontal orientation. This pivotal
302 moment marks the shift in operational dynamics as the UAV transitions from hover to fixed-wing

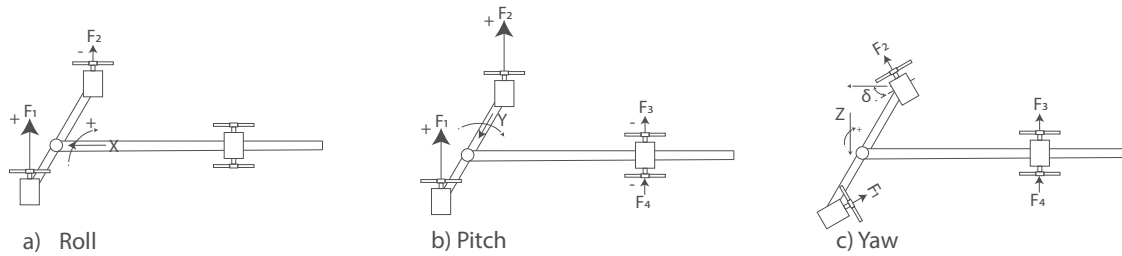


Figure 14. Diagram of tilting Mechanism at low speed flight.

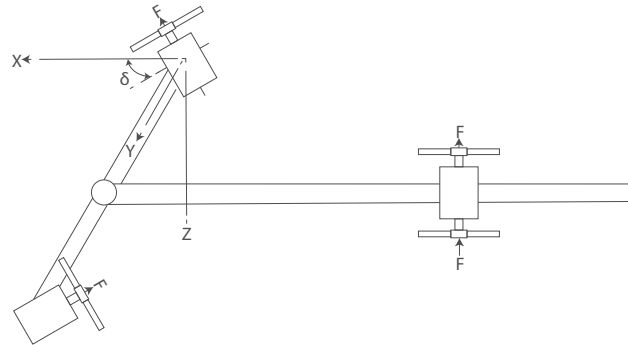


Figure 15. Tilting Mechanism Frame.

303 mode. Unlike traditional aircraft configurations, where control surfaces such as ailerons, elevators, and
 304 rudders govern maneuverability, this CUAV employs a unique motion for the frontal tilting rotors.

305 This innovative approach streamlines the control system and enhances maneuverability and
 306 responsiveness during flight, rotor motion are defined at figure 15 which allows having such responsive,
 307 adding that is placed on strategy point to performed a wing change of angle. By eschewing traditional
 308 control surfaces, the UAV achieves unprecedented agility and precision, enabling it to execute swift and
 309 intricate maneuvers with remarkable ease. The absence of control surfaces eliminates the associated
 310 mechanical complexities and aerodynamic constraints, allowing the UAV to push the boundaries of
 311 aerial maneuverability and operational performance.

312 Furthermore, using a dual-mode capability, combining VTOL and fixed-wing flight, maximizes
 313 mission efficiency and versatility. During VTOL operations, the frontal rotors provide lift and control
 314 for take-offs, landings, and low-speed flight, ensuring operational flexibility in confined or challenging
 315 environments. Conversely, in cruise flight mode, the transition to horizontal rotor orientation optimizes
 316 aerodynamic efficiency, leveraging the fixed-wing configuration for sustained flight and extended
 317 mission endurance, see Figure 16.

318 2.4. Manufacturing

319 This innovative convertible UAV boasts a lightweight wing crafted using additive manufacturing,
 320 a cutting-edge technique known as 3D printing. This method allows for the incorporation of multiple
 321 materials within the wing structure. By strategically integrating these materials, the engineers achieved
 322 an incredibly lightweight without sacrificing strength. However, the benefits of additive manufacturing
 323 extend beyond the wing itself. This technology also facilitated the creation of a lattice structure within
 324 the wing. Lattice structures, resembling a complex web, offer exceptional strength-to-weight ratios,
 325 further contributing to the overall lightness of the UAV.

326 This lightweight design does not come at the expense of functionality. Thanks to additive
 327 manufacturing, the entire mechanism and avionics are seamlessly integrated within the interior of
 328 the wing. This ingenious approach frees up space and further streamlines the overall design of the
 329 convertible UAV.

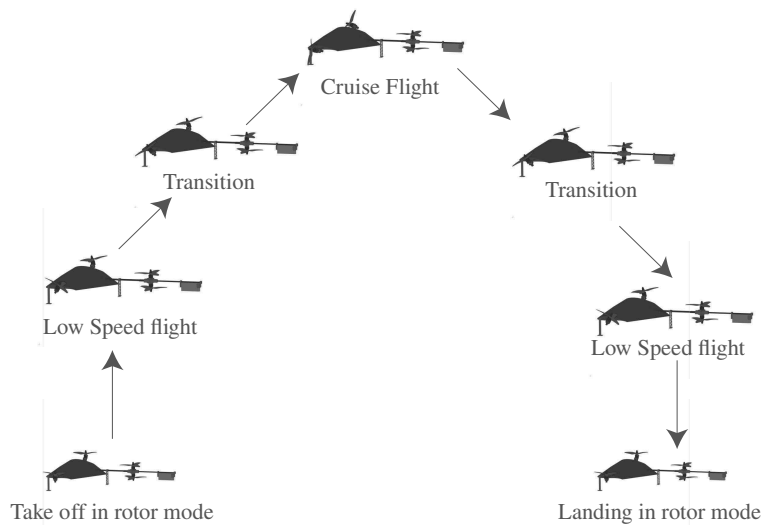


Figure 16. Hybrid Mission.

330 The structural studies presented in Figures 6 and 8 aim to address the SIMP by strategically
 331 distributing bars along the wing to manage the forces. These studies were influenced by additive
 332 manufacturing techniques, specifically the interaction between walls and infill. However, in this case,
 333 these techniques served merely as inspiration. The structural points were determined based on the
 334 pressure distribution required at each point and a simplification of the SIMP algorithm, which only
 335 placed at this case pressure point, filled by mechanical bars for this case, and strategically distributed
 336 and filled with double the nozzle size to have a rigid structure.

337 As seen in Figure 17, this prototype utilized an improved and simplified structure that handles
 338 the forces as shown in Figure 6 and achieves maximum lightness.

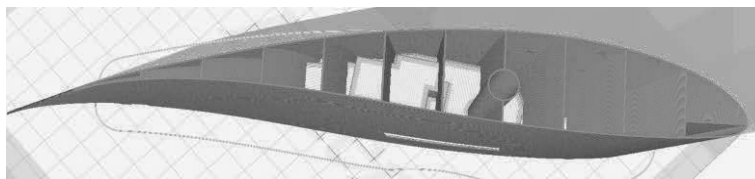


Figure 17. Internal 3D printed Wing structure

339 Optimization and the use of multiple materials were key factors in the creation of the wing, as
 340 depicted in Figure 18. Several techniques were tested, but ultimately, a lattice polymeric structure, as
 341 seen in Figure 17, was chosen. Different patterns and materials exhibit different behaviors, but for this
 342 application, load distribution, as previously mentioned in Figure 6 and 8, guided the selection of the
 343 final approach.

344 ABS is renowned for its excellent mechanical properties, particularly its high stiffness. This makes
 345 it an ideal choice for applications requiring durable and robust components. One of the significant
 346 advantages of ABS is its ability to withstand higher temperatures without deforming. ABS has a glass
 347 transition temperature of approximately 105°C, which is significantly higher than PLA's 60°C and
 348 PETG's 80°C. This high thermal resistance ensures that ABS-printed parts maintain their shape and
 349 structural integrity under heat, making them suitable for a wider range of applications. ABS typically
 350 has a tensile strength of 40-50 MPa, while PLA ranges from 37-50 MPa, and PETG ranges from 48-55
 351 MPa, giving us the best performance for this application

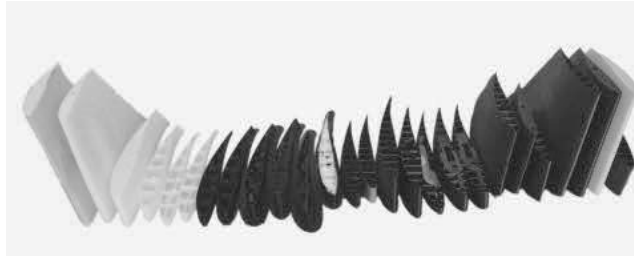


Figure 18. Multiple techniques used for Wing.

352 2.5. Performance

353 Convertible aircraft, with their ability to transition between fixed-wing and rotary-wing modes,
 354 present unique challenges in performance evaluation. Unlike conventional aircraft, their performance
 355 is influenced by a complex interplay of factors, including airspeed, altitude, tilt angle, and payload. A
 356 comprehensive understanding of these interactions is crucial for optimizing aircraft design, operation,
 357 and mission planning.

358 The VN diagram, a fundamental tool in aerospace engineering, plays a crucial role in the design
 359 and operational planning of convertible UAVs. The VN diagram visually represents the relationship
 360 between an aircraft speed (V) and the load factor (N), providing engineers with critical insights into the
 361 aircraft's flight envelope. This diagram serves as a blueprint for understanding permissible operating
 362 limits across different flight modes for convertible UAVs.

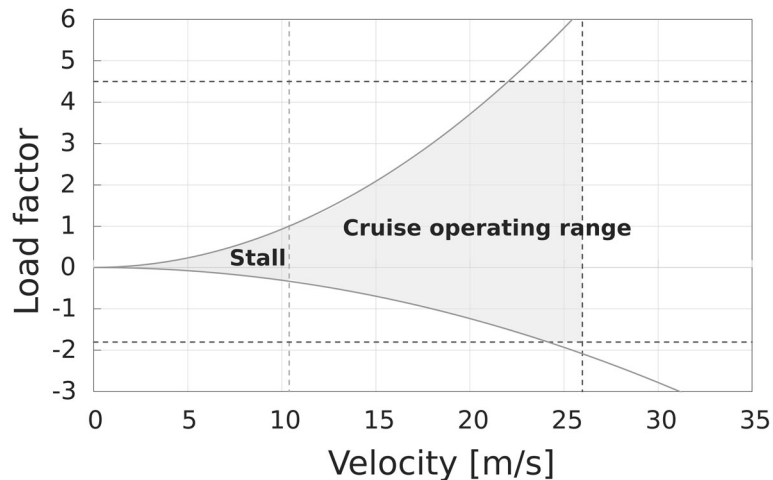


Figure 19. Flight envelope.

363 This diagram provides a clear visualization of the operational limits of the airfoil under different
 364 load factors and velocities, represented in Figure 19. The VN diagram analysis of our aircraft design
 365 demonstrates a well-defined range of operation, ensuring both safety and performance during various
 366 flight conditions. The evaluation indicates that the aircraft operates effectively within a speed range of
 367 10 to 25 meters per second (m/s), allowing for a versatile flight envelope.

368 The aircraft's stall speed (V_s) at 1g, or level flight, is calculated to be approximately 10 m/s. This
 369 speed marks the minimum velocity at which the aircraft can sustain level flight without stalling. On
 370 the other end, the maximum structural speed (V_{max}) is determined to be 25 m/s. Beyond this speed,
 371 there is a risk of structural damage, and the aircraft should not be operated at these velocities.

372 The positive load factor limit of the aircraft is evaluated to be +4.4g, while the negative load factor
 373 limit is -1.76g. These load factor limits indicate the maximum g-forces the aircraft can safely withstand
 374 during positive and negative maneuvers. The stall speed increases at higher load factors, such as

375 during sharp turns or sudden climbs. For instance, at a 2g load factor, the stall speed increases to
 376 approximately 15.6 m/s, ensuring the aircraft remains stable and controllable even during aggressive
 377 maneuvers.

378 The VN diagram assessment confirms that the aircraft design provides a robust operational
 379 range from 10 to 25 m/s. This range not only supports stable and efficient cruise conditions but also
 380 accommodates various maneuvering needs, including steep turns and climbs, without compromising
 381 safety. For a convertible UAV with tilting rotors, the performance surface showcases how the available
 382 payload varies with different velocities and rotor tilt angles, by that reason it is developed, see Figure
 383 20.

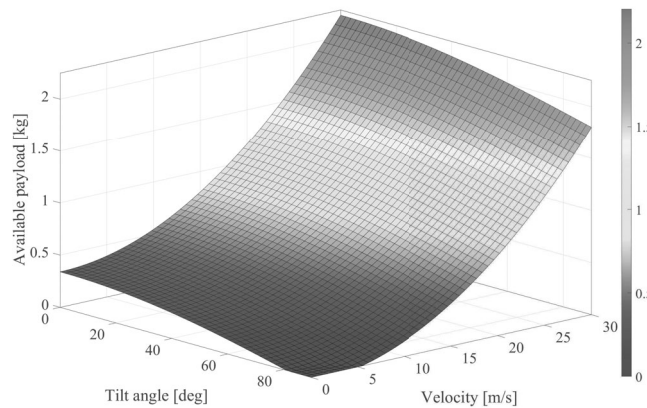


Figure 20. Performance surface for variation of the payload for each state.

384 The UAV is most efficient in forward flight, offering the highest payload capacity. This analysis
 385 optimizes the UAV operation for different missions, ensuring maximum payload capability while
 386 maintaining safe and efficient flight characteristics. The maximum payload is determined by the
 387 maximum hover take-off, limited by rotor forces, restricting the aircraft to 1.1kg if the payload is at the
 388 center of mass for balanced force distribution. Figure 20 shows the system performance in each phase.

389 In hover mode with rotors fully tilted (0 deg), the UAV consumes more power, limiting the
 390 available payload to 0.4 kg. The UAV achieves better efficiency at a 45 deg rotor tilt and 20 m/s speed,
 391 allowing for a slightly higher available payload of 0.8 kg. The UAV reaches optimal efficiency in
 392 forward flight mode with rotors at 90 deg tilt, providing the highest available payload of 0.6 kg at
 393 14m/s.

394 3. Modeling and stabilization

395 In this section, the equations of motion that govern the dynamic behaviors of CUAV are
 396 described. The mathematical framework, Newton-Euler equations, are used to model system dynamics,
 397 acknowledging the simplifications and assumptions inherent in these models.

398 The choice of reference frames is crucial in defining the 3D motion of the vehicle relative to its
 399 environment. The North-East-Down (NED) convention is considered, which is widely employed in
 400 aerospace applications and the axes system involves the special Euclidean group $SE(3)$. By examining
 401 the properties of $SE(3)$ and its implications for reference frame transformations, the algorithm of
 402 guidance, navigation, and control is proposed. Note that those three reference frames are established
 403 to obtain the mathematical model of the aerial vehicles; see Figure 23.

404 For the vehicle orientation, Euler angles are defined as, ϕ is an angle defined between x_B axis
 405 and a resultant plane from y_I and z_I ; θ is an angle defined between y_B axis and a resultant plane from
 406 x_I and z_I , and ψ is an angle defined between z_B axis and a resultant plane from x_I and y_I . Those
 407 definitions allow aircraft to obtain attitude stabilization in a 3D space. In this sense, two angles that

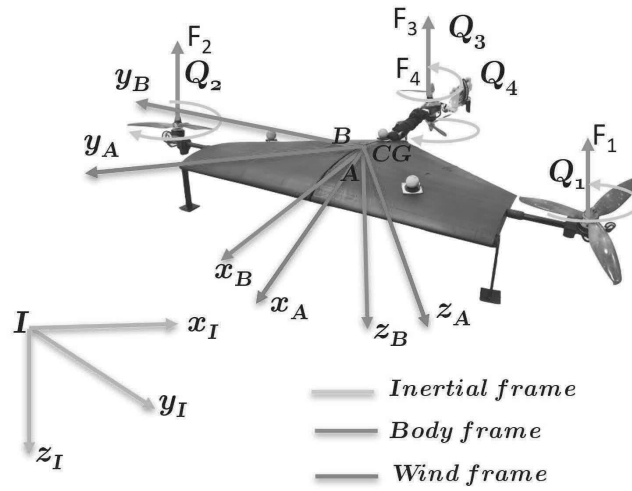


Figure 21. References frames of the CUAV.

408 provide the information in the aerodynamic or wind frame are the angle of attack α , and the sideslip
 409 angle β .

410 For the tilting-rotor system of proposed aircraft, an auxiliary tilting frame or rotating frame is
 411 defined about y_R , with x_{R_1} , z_{R_1} , x_{R_2} , and z_{R_2} as the principal axes, with tilting angles δ_{R_1} and δ_{R_2}
 412 as shown in Figure 22. The upwards position is 0 deg while the forward position is $-\frac{\pi}{2}$ deg according to
 413 the NED (North-East-Down) convention and the right-hand rule.

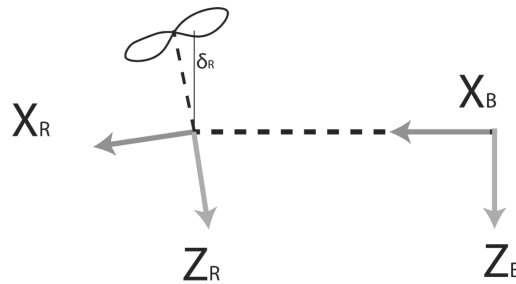


Figure 22. References frame for angular rotation.

414 3.1. Equations of motion

415 The model of the vehicle considers an inertial fixed frame as $\mathcal{I} = \{x_I, y_I, z_I\}$ and a body
 416 frame fixed attached to the center of gravity of the vehicle as $\mathcal{B} = \{x_B, y_B, z_B\}$. The wind frame
 417 $\mathcal{A} = \{x_A, y_A, z_A\}$ is considered during the forward flight [32], (see 23). The configuration of the
 418 convertible UAV is defined by the location of the center of gravity and the attitude with respect to the
 419 inertial frame. Then, the configuration manifold is the special Euclidean group $SE(3)$, which is the
 420 semidirect product of \mathbb{R}^3 and the special orthogonal group $SO(3)$.

421 The Newton-Euler formulation, for rigid body, is used in order to obtain the mathematical model
422 as

$$\dot{\zeta} = V \quad (1)$$

$$m\dot{V} = RF + mge_3 + D_{\zeta}(t) \quad (2)$$

$$\dot{R} = R\hat{\Omega} \quad (3)$$

$$J\dot{\Omega} = -\Omega \times J\Omega + \tau_a + D_{\eta}(t) \quad (4)$$

where $\zeta = (x, y, z)^{\top} \in \mathbb{R}^3$ and $V = (v_x, v_y, v_z)^{\top} \in \mathbb{R}^3$ are the position coordinates and translational velocity relative to the inertial frame. $\eta = (\phi, \theta, \psi)^{\top} \in \mathbb{R}^3$ describes the rotation coordinates where ϕ, θ , and ψ represent the roll, pitch, and yaw or heading, respectively. e_1, e_2 , and e_3 are the vectors of the canonical basis of \mathbb{R}^3 in \mathcal{I} . The rotation matrix, $R \in \text{SO}(3) : \mathcal{B} \rightarrow \mathcal{I}$, satisfies the $\text{SO}(3) = \{R \mid R \in \mathbb{R}^{3 \times 3}, \det[R] = 1, RR^{\top} = R^{\top}R = I\}$ and is parameterized by the Euler angles ϕ, θ , and ψ . The rotation matrix is written as

$$R = \begin{pmatrix} c_{\theta}c_{\psi} & s_{\phi}s_{\theta}c_{\psi} - c_{\phi}s_{\psi} & c_{\phi}s_{\theta}c_{\psi} + s_{\phi}s_{\psi} \\ c_{\theta}s_{\psi} & s_{\phi}s_{\theta}s_{\psi} + c_{\phi}c_{\psi} & c_{\phi}s_{\theta}s_{\psi} - s_{\phi}c_{\psi} \\ -s_{\theta} & s_{\phi}c_{\theta} & c_{\phi}c_{\theta} \end{pmatrix}$$

423 where the shorthand notation of $s_a = \sin(a)$ and $c_a = \cos(a)$ is used. $\Omega = (p, q, r)^{\top} \in \mathbb{R}^3$ is the angular
424 velocity in \mathcal{B} , where the hat map $\hat{\cdot} : \mathbb{R}^3 \rightarrow \mathfrak{so}(3)$ is defined by the condition that $\hat{a}b = a \times b$ for all
425 $a, b \in \mathbb{R}^3$.

$$\hat{\Omega} = \begin{pmatrix} 0 & -r & q + \delta_{R_1} \\ r & 0 & -p - \delta_{R_2} \\ -q - \delta_{R_1} & p + \delta_{R_2} & 0 \end{pmatrix} \quad (5)$$

426 where δ_{R_1} and δ_{R_2} are the tilting angles.

427

428

The forces acting on the body frame are described as follows:

$$F = \begin{bmatrix} F_{x_B} \\ F_{y_B} \\ F_{z_B} \end{bmatrix} = \begin{bmatrix} 0 \\ 0 \\ -F_3 \end{bmatrix} + \begin{bmatrix} 0 \\ 0 \\ -F_4 \end{bmatrix} + \begin{bmatrix} -F_1 \sin(\delta_{R_1}) \\ 0 \\ -F_1 \cos(\delta_{R_1}) \end{bmatrix} + \begin{bmatrix} -F_2 \sin(\delta_{R_2}) \\ 0 \\ -F_2 \cos(\delta_{R_2}) \end{bmatrix} \quad (6)$$

429 where $F = (F_{x_B}, F_{y_B}, F_{z_B})^{\top} \in \mathbb{R}^3$ is the vector of the total forces in the x, y , and z axes respectively. F_i is
430 the lift force or thrust force of the propeller for $i = 1, 2, 3, 4$.

431

432

In hover mode ($\delta_{R_1} = 0$ and $\delta_{R_2} = 0$), the (6) becomes

$$F = \begin{bmatrix} F_{x_B} \\ F_{y_B} \\ F_{z_B} \end{bmatrix} = \begin{pmatrix} 0 \\ 0 \\ -(F_1 + F_2 + F_3 + F_4) \end{pmatrix} \quad (7)$$

433 In cruise mode ($\delta_{R_1} \approx \frac{\pi}{2}$ and $\delta_{R_2} \approx \frac{\pi}{2}$), the (6) becomes

$$F = \begin{bmatrix} F_{x_B} \\ F_{y_B} \\ F_{z_B} \end{bmatrix} = \begin{pmatrix} -(F_1 + F_2) \\ 0 \\ -(F_3 + F_4) \end{pmatrix} \quad (8)$$

434 For external forces, are include specially aerodynamics ones, defining them as:

$$D_{\zeta} = \begin{pmatrix} d_{\zeta_1} \\ d_{\zeta_2} \\ d_{\zeta_3} \end{pmatrix} = RW^T \begin{pmatrix} D_a \\ Y_a \\ L_a \end{pmatrix} \quad (9)$$

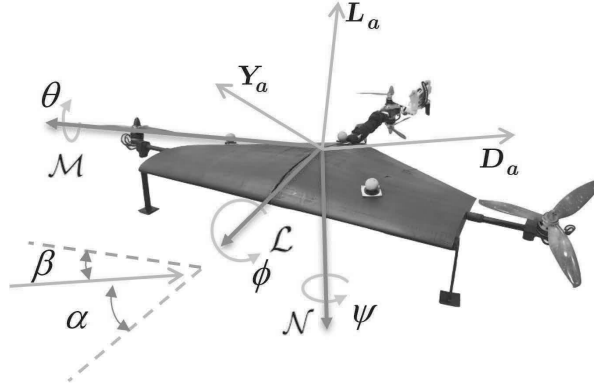


Figure 23. References frames of the CUAV.

435 with the rotation aerodynamic matrix $W : \mathcal{B} \rightarrow \mathcal{A}$ that transforms a force from the body frame to
436 aerodynamic frame is described as

$$W = \begin{pmatrix} c_{\alpha}c_{\beta} & s_{\beta} & s_{\alpha}c_{\beta} \\ -c_{\alpha}s_{\beta} & c_{\beta} & -s_{\alpha}s_{\beta} \\ -s_{\alpha} & 0 & c_{\alpha} \end{pmatrix}$$

437 where α is the angle of attack and β are the sideslip angle. L , Y , and D are the aerodynamic forces: lift,
438 side force, and drag, respectively, [32].

439 In the context of torque analysis within the aircraft dynamics, the torque vector τ_a is defined at the
440 center of gravity with a pivotal point corresponding to the body frame. This representation provides
441 the rotational dynamics of the aircraft and is derived from the collective effects of the four-rotor forces.
442 This torque is formulated as follows:

$$\tau_a = \begin{pmatrix} \tau_{\phi} \\ \tau_{\theta} \\ \tau_{\psi} \end{pmatrix} = \begin{pmatrix} d(F_1 - F_2) \\ l_2(F_3 + F_4) - l_1(F_1 + F_2) + \tau_{wing} \\ Q_1 + Q_3 - Q_2 - Q_4 + F_1 \sin(\delta_{R_1}) - F_2 \sin(\delta_{R_2}) \end{pmatrix} \quad (10)$$

443 where $\tau_{wing} = C_{M,wing} \frac{1}{2} \rho V^2 S_{wing} c_{wing} \Delta\alpha$ is encompassed the contributions stemming from the frontal
444 wing with $C_{m,wing}$ that is the pitching moment coefficient of the wing, ρ is the air density, V is the
445 airspeed of the aircraft, S_{wing} is the wing area, c_{wing} is the average chord length of the wing, and $\Delta\alpha$ is
446 the change in angle of attack of the wing. $Q_i = \rho A_i r_i^3 c_{Q_i} \omega_i^2$, where A_i is the rotor disk area, r_i is the
447 rotor radius, c_{Q_i} denotes the rotor shaft moment coefficient and ω_i denotes the angular velocity of the
448 rotor i with $i=1, 2, 3, 4$. d stands for arm length, l_1 and l_2 for distances to the center of mass.

449 The moments acting on the aerial vehicle are described

$$D_{\eta} = \begin{pmatrix} d_{\eta_1} \\ d_{\eta_2} \\ d_{\eta_3} \end{pmatrix} = d_{\eta_{gyro}} + d_{\eta_{aero}} \quad (11)$$

450 The gyroscopic moment generated by the rotation of the airframe and the four rotors is described by

$$d_{\eta gyro} = \sum_{k=1}^4 (-1)^{k+1} I_{r_k} [\Omega \times e_3 \omega_k] \quad (12)$$

451 Finally, the *aerodynamic moments* presented on the airframe are described as

$$d_{\eta aero} = \begin{pmatrix} \mathcal{L} & \mathcal{M} & \mathcal{N} \end{pmatrix}^T$$

452 where \mathcal{L} , \mathcal{M} and \mathcal{N} are the aerodynamic rolling, pitching and yawing moments respectively. [32], [5].

453 Using Equations(1)–(4), a nonlinear set of equations can be described as:

$$\begin{aligned} \dot{x} &= v_x \\ \dot{y} &= v_y \\ \dot{z} &= v_z \\ \dot{v}_x &= \frac{F_{x_B}}{m} (c_\theta c_\psi) + \frac{F_{y_B}}{m} (s_\phi s_\theta c_\psi - c_\phi s_\psi) + \frac{F_{z_B}}{m} (c_\phi s_\theta c_\psi + s_\phi s_\psi) + d_{\xi_1} \\ \dot{v}_y &= \frac{F_{x_B}}{m} (c_\theta s_\psi) + \frac{F_{y_B}}{m} (s_\phi s_\theta s_\psi + c_\phi c_\psi) + \frac{F_{z_B}}{m} (c_\phi s_\theta s_\psi - s_\phi c_\psi) + d_{\xi_2} \\ \dot{v}_z &= \frac{F_{x_B}}{m} (-s_\theta) + \frac{F_{y_B}}{m} (s_\phi c_\theta) + \frac{F_{z_B}}{m} (c_\phi c_\theta) + g + d_{\xi_3} \\ \dot{\phi} &= p + q \sin(\phi) \tan(\theta) + r \cos(\phi) \tan(\theta) \\ \dot{\theta} &= q \cos(\phi) - r \sin(\phi) \\ \dot{\psi} &= q \sec(\theta) \sin(\phi) + r \sec(\theta) \cos(\phi) \\ \dot{p} &= \left(\frac{J_{yy} - J_{zz}}{J_{xx}} \right) qr + \left(\frac{1}{J_{xx}} \right) \tau_\phi + d_{\eta 1} \\ \dot{q} &= \left(\frac{J_{zz} - J_{xx}}{J_{yy}} \right) pr + \left(\frac{1}{J_{yy}} \right) \tau_\theta + d_{\eta 2} \\ \dot{r} &= \left(\frac{J_{xx} - J_{yy}}{J_{zz}} \right) pq + \left(\frac{1}{J_{zz}} \right) \tau_\psi + d_{\eta 3} \end{aligned} \quad (13)$$

454 **Remark 1.** As the rotation of the four propellers on the convertible UAV is balanced, the gyroscopic moment
455 will essentially be zero. The only cases in which gyroscopic moments will not be zero are if there is a significant
456 difference in the RPM of the four motors and the presence of a strong sideways cross-wind.

457 **Remark 2.** The design of the convertible UAV is based on in a configuration that optimizes the aerodynamic
458 properties and reduces drag forces, which provides steady flights. In addition, the wing involves a damping that
459 reduces the transient or oscillatory motion, specifically unstable spiral roll.

460 Based on the remarks, the disturbance terms D_η and D_ξ satisfy the linear growth bound as
461 $\| D_\xi \| \leq c_\xi \forall t$ and $\| D_\eta \| \leq c_\eta \forall t$.

462 3.2. Guidance, navigation and control algorithm

463 The guidance, navigation, and control of the convertible UAV is based on a geometric tracking
464 control in SE(3), (special Euclidean group), see [33]. The control is a saturated proportional, integral,
465 and derivative (PID) and provides smooth trajectory tracking based on SE(3), even in the presence of
466 wind disturbances. For this purpose, the equations (13) can be rewritten as

467 For this purpose, the equations (13) can be rewritten as

$$\dot{\xi} = V \quad (14)$$

$$\dot{V} = u_n + d_\xi(t) \quad (15)$$

$$\dot{R} = R\hat{\Omega} \quad (16)$$

$$\dot{\Omega} = u_a + d_R(t) \quad (17)$$

468 where $u_n \in \mathbb{R}^3$ and $u_a \in \mathbb{R}^3$ are virtual control inputs for the position and orientation dynamics.
 469 $d_{\xi}(t) = \frac{D_{\xi}(t)}{m}$ and $d_R(t) = J^{-1}[-\Omega \times J\Omega + D_{\eta}(t)]$.

470 For a smooth transition, a condition is defined in order to ensure that, at each instant of time, at
 471 most one of the two control inputs is active. The geometric navigation considers a guidance frame that
 472 is designed to perform autonomous flights with a convergence to the contour of the task with small
 473 normal velocity.

$$u_n = u_{n1}g_1(t) + u_{n2}f_1(t) \quad (18)$$

$$f_1(t) = \begin{cases} 0 & \text{for } 0 \leq t < T_1 \\ 1 & \text{for } T_1 \leq t \leq T_F \end{cases} \quad \text{with } g_1(t) = 1 - f_1(t) \quad (19)$$

474 For hover flight, $0 \leq t < T_1$, the virtual control input u_{n1} is defined as

$$u_{n1} = ge_3 - \frac{RF}{m} \quad (20)$$

475 For cruise mode, $T_1 \leq t \leq T_F$, the virtual control input u_{n2} is defined as

$$u_{n2} = ge_3 - \frac{RF}{m} \quad (21)$$

476 For orientation dynamics, the virtual control input u_a is defined as

$$u_a = J^{-1}\tau_a \quad (22)$$

477 **Remark 3.** The transition maneuver of the CUAV, from hover to cruise modes and vice versa, is smooth, and it
 478 starts when the vehicle reaches the hovering flight in the initial or actual waypoint, i.e., $F_{zB} \approx mg$; after that the
 479 transition starts, and the cruise mode is performed until the CUAV arrives to the final waypoint to return to the
 480 hovering flight.

481 **Definition 1.** A guidance frame $\mathcal{G} = \{f_g, b_g, n_g\}$ is a reference frame that consists of the control forward vector
 482 f_g , the control binormal vector b_g and the control normal vector n_g . This frame satisfies the NED (North East
 483 Down) system and considers the terminology from the names of the three unit vectors in the reference frame for a
 484 curve in \mathbb{R}^3 .

485 The three vectors are defined as follows (for more details see [33]):

- 486 • The control normal vector n_g is defined as a function of the position and velocity errors.

$$n_g = \frac{ge_3 - u_n}{\|ge_3 - u_n\|} \quad (23)$$

- 487 • The control forward vector f_g is defined as a unit vector in the (n_g, t_d) plane and is orthogonal to
 488 n_g such as $n_g \cdot t_d > 0$ with $t_d = \frac{\dot{\xi}_d}{\|\dot{\xi}_d\|}$. Then

$$f_g = \frac{n_g \times e_1}{\|n_g \times e_1\|} \quad (24)$$

- 489 • The control binormal vector b_g is defined as

$$b_g = -(f_g \times n_g) \quad (25)$$

490 **Definition 2.** A desired rotation matrix $R_d \in SO(3)$ is defined as $R_d = [f_g \ b_g \ n_g]$ corresponding to reference
 491 frame or guidance frame where $f_g = R_d e_1$, $b_g = R_d e_2$ and $n_g = R_d e_3$.

492 From [33] is well-known the next statements.

- 493 1. $u_n \neq g e_3$
- 494 2. n_g is a well-defined unit vector.
- 495 3. f_g is a well-defined unit vector.
- 496 4. $\{f_g \ b_g \ n_g\}$ is orthonormal and the matrix $R_d = [f_g \ b_g \ n_g]$

497 Establishing a guidance frame enables the development of a control strategy that allows the
 498 introduction of u_n as an input while utilizing position references as feedback. In this case, a classical
 499 Proportional, Integral, and Derivative (PID) control scheme is proposed. A navigation scheme using
 500 this type of control can be effective, providing accurate feedback and a sufficiently responsive system.
 501 For this purpose, the following PID saturated structure is utilized, [34].

502 The position control for the CUAUV is proposed as follows:

$$u_n = \text{Sat} \left(k_{p_{\zeta}} e_{\zeta} + k_{d_{\zeta}} \dot{e}_{\zeta} + k_{i_{\zeta}} \int e_{\zeta} dt \right) \quad (26)$$

503 where $e_{\zeta} = \zeta_d - \zeta$, $\dot{e}_{\zeta} = \dot{\zeta}_d - \dot{\zeta}$ are the position and velocity errors. $k_{p_{\zeta}}$, $k_{d_{\zeta}}$ and $k_{i_{\zeta}}$ stand for the
 504 diagonal, and positive definite matrices. The stability analysis of this saturated control can be found in
 505 [35]

506 The similar procedure is used to propose the control to orientation dynamics, u_a , considering
 507 the rotation desired matrix $R = [f_g \ b_g \ n_g]$, that correspond to reference frame. Based on the
 508 group operation of SO(3), the attitude and the angular velocity errors are defined as $R_e = RR_d^T$ and
 509 $e_{\Omega} = \Omega_d - \Omega$.

510 The orientation control is described as

$$u_n = \text{Sat} \left(k_{p_{\Omega}} e_R + k_{d_{\Omega}} \dot{e}_{\Omega} + k_{i_{\Omega}} \int e_R dt \right) \quad (27)$$

511 where $e_R = \text{Skew}(RR_d^T)^{\vee}$, with $\text{Skew}(A) = \frac{1}{2}(A - A^T)$ and the operator $(\cdot)^{\vee}$ is the inverse of the
 512 “hat” operator (for the definition of asymptotic tracking on manifolds, see). $k_{p_{\Omega}}$, $k_{d_{\Omega}}$ and $k_{i_{\Omega}}$ stand for
 513 the diagonal, and positive definite matrices, [33].

514 A dual-layer controller architecture is utilized to enhance the navigation and attitude control of
 515 the convertible aircraft. This approach comprises two distinct layers. The first layer focuses on rate
 516 control, using velocity for translational motion and angular velocity for rotational motion. The second
 517 layer is dedicated to position control for translational motion and attitude control for rotational motion.
 518 By combining both layers, the system produces a final output that effectively guides the aircraft.

519 The dual-layer controllers follow the same structure previously mentioned but with a hierarchical
 520 arrangement. Instead of explicitly presenting the equations, the interaction between the two layers
 521 is emphasized for clarity. This arrangement ensures smooth integration and coordination between
 522 rate and position control, enabling precise and responsive navigation and attitude control for the
 523 convertible aircraft, see Figure 24.

524 4. Real-time validation

525 In order to validate the vehicle and the proposed GNC algorithm, a design of experiments (DoE) is
 526 executed in indoor environment, performing the capabilities of the proposed system. The experiments
 527 focus on trajectory tracking tests, which facilitate the assessment of the system performance under
 528 consistent patterns and diverse movement combinations. However, specific missions are performed
 529 for convertible aircraft to evaluate the system across various scenarios.

530 The tests are carried out in the Navigation Laboratory at the Aerospace Engineering Research
 531 and Innovation Center of the Faculty of Mechanical and Electrical Engineering at the Autonomous
 532 University of Nuevo Leon. This laboratory features 16 VICON T-40 cameras to obtain the localization
 533 measurements; see Figure 25.

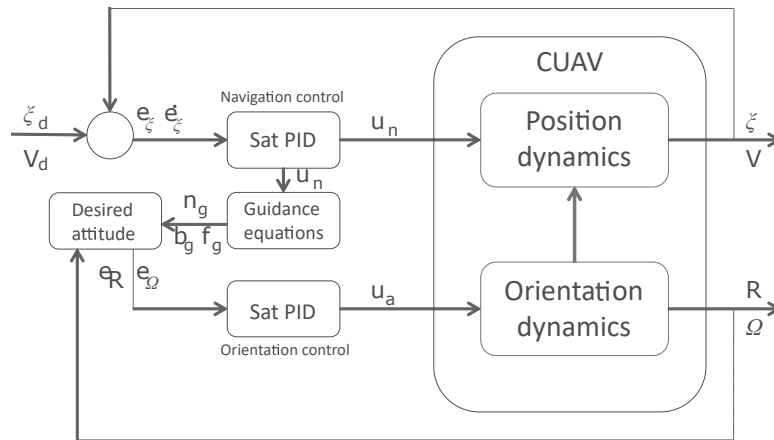


Figure 24. Guidance, navigation and control scheme for the CUAV.

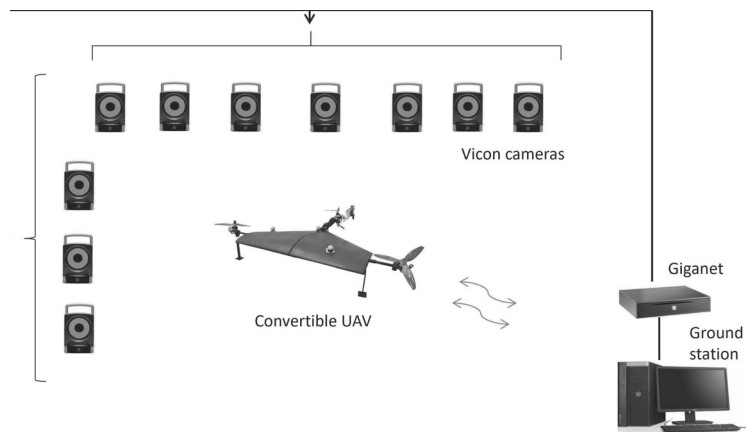


Figure 25. Tracking system.

534 The ground station receives and sends the information to the autopilot systems, and the interface
 535 is developed in order to graph the state variables of the system, see Figure 26.

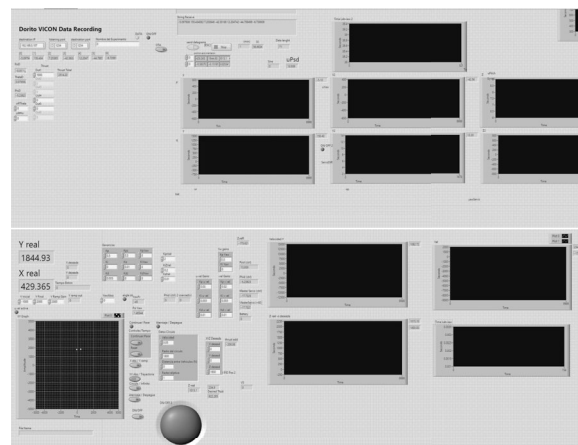


Figure 26. CUAV interface in the ground station.

536 The proposed CUAV is equipped with a low-cost avionics system developed by our laboratory,
 537 allowing us to access the whole state variables of the system. For the inner loop, the attitude is obtained
 538 via the estimation method, i.e., the complementary filter in SE(3), while for the outer loop, the position

539 is obtained through estimation by the tracking system. The scheme of the aircraft is shown in Figure 27,
 540 providing a homemade autopilot in order to manipulate the complete systems for flights in real-time.
 541 For that reason, it is possible to debug the system on each of its steps, and Figure 28 illustrates the
 542 real-time experiments.

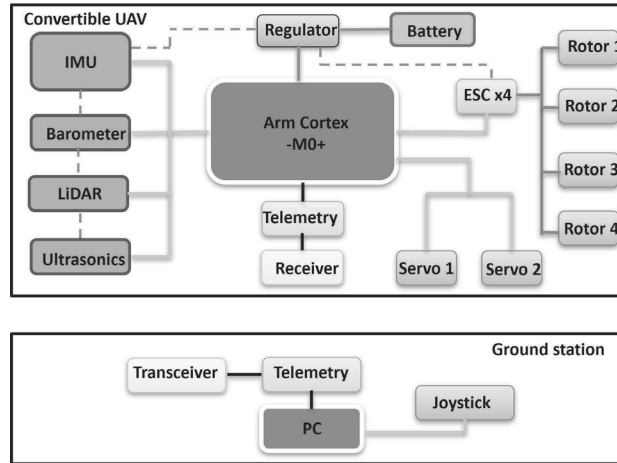


Figure 27. Flight computer scheme.

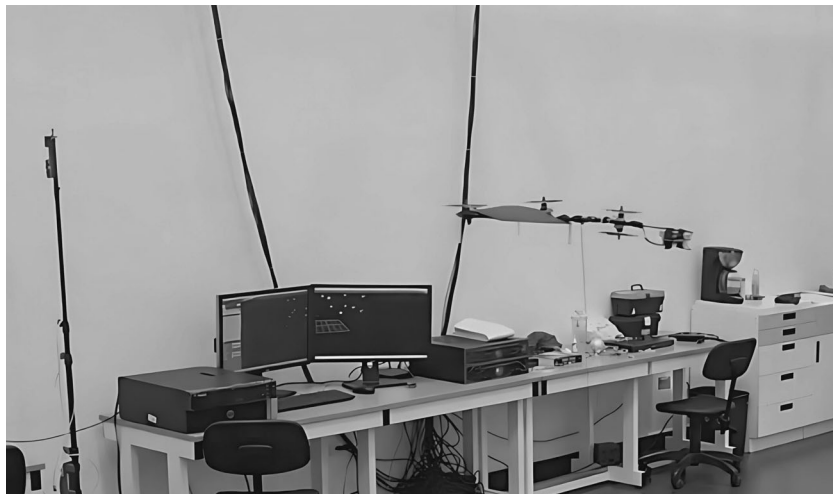


Figure 28. Real-time flight of the CUAV.

543 The experiments are executed for this prototype enable the characterization of the system and the
 544 identification of unexpected behaviors. In this sense, specific paths and input ramp signals are selected
 545 for testing. Notably, these experiments are run in real-time, and the information about state variables is
 546 sent to the ground station. The camera system is essential for data tracking, requiring using a bounded
 547 environment for experimentation. Despite these constraints, the selected paths and input ramps
 548 provide valuable insights into the system performance and behavior under controlled conditions. The
 549 information is tracked during this experiment, including position data, sensor readings, and control
 550 inputs, which are recorded in a data file for analysis.

551 Experiments selected are those represented on table 4.

552 4.1. Circle

553 For the circular trajectory, it has selected a circle with a radius of 1750 mm, a height of 1800 mm,
 554 and a velocity of 0.03 rev/s. For this case, the tilting mechanism is assessed, which allows us to have

Experiment	Description
Circle	Circle pattern with tangent tracking, fixed Z, and multiple experiments development for dependence on velocity analyze
Infinite	Complex pattern for whole system test, combined capabilities are test
Tilting Ramp	Tilting rotor test for control test, where required an input similar to a forward flight with a process of stopping at the end of the path
Fast line	Test for max linear velocity on controlled environmental

Table 4. Design of experiments

555 that type of motion without using input on the rotors; those are only controlled by the mixer for
 556 stabilization purposes.

557 Geometrical errors, a natural consequence of the lower resolution on actuators, are a significant
 558 factor in our trajectory. These errors are visualized by a circle made of trajectories based online. Despite
 559 these challenges, the trajectory remains within correct values, with some drift but an acceptable
 560 tracking error, see Figure 29.

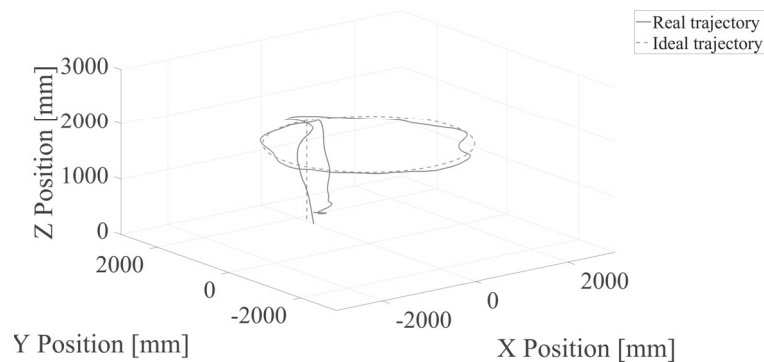


Figure 29. XYZ trajectory tracking, real vs ideal.

561 One of the objective of this design is to ensure that the pitch angle is as small as possible, especially
 562 so as not to interfere with the forces generated by the wing. As a result, it is shown that the system
 563 follows the system with 100mm of maximum error and ± 3 on angle error; it is shown in Figure 30.

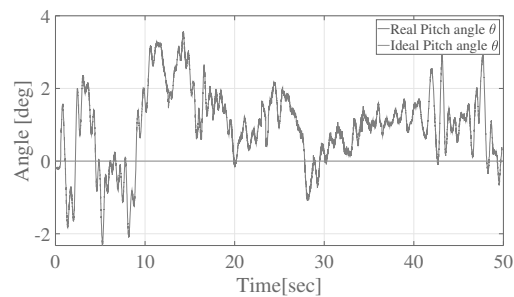


Figure 30. Pitch angle, real vs ideal (low pitch)

564 4.2. Infinite

565 While the circular path experiment provides valuable insights into maintaining a constant radius,
 566 a separate experiment simulating an infinite straight path is equally important. This allows us to
 567 evaluate the system ability to handle long-distance navigation and drift correction, which is crucial
 568 for real-world applications like long-range surveillance. A complex trajectory is tested for an infinite
 569 trajectory, and a control signal response is illustrated; see Figure 31.

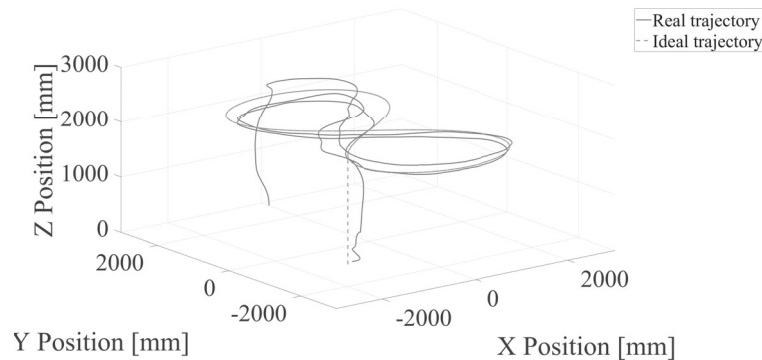


Figure 31. XYZ trajectory tracking, real vs ideal.

570 As seen before, the CUAV accomplishes and follows this trajectory with a deviation of 200mm;
 571 behavior expected because the system is performing a transition phase, which involves uncertainty to
 572 be solved for the proposed GNC algorithm. The form control field shows that the system is tracking
 573 signals; errors are expected from external sensor data, see Figure 32

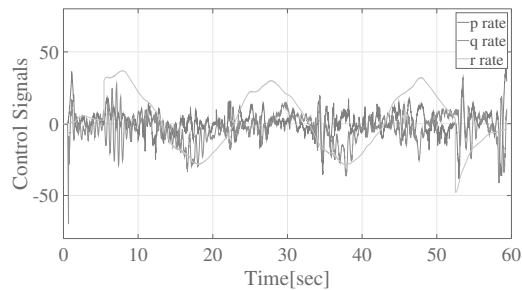


Figure 32. Control signals on Infinite trajectories.

574 4.3. Tilting Ramp

575 This experiment shows the fast transition of the system on a tilting rotor, where the input is a fast
 576 change on tilting angles, as shown in Figure 33.

577 For this case, a straight line is developed to change between hover and cruise flight.

578 In this short-period experiment, the control scheme compensates for height loss. Also, it
 579 accelerates the CUAV, performing a maximum of 2 m/s, where it is realized that the system is
 580 still in hover mode, and rotors do not make the whole change. However, it is a short-period experiment
 581 showing the expected accomplishment of dynamics, see Figure 34.

582 As seen in Figure 35 at 10 to 12 seconds, the system increases lift, which is directly seen as a
 583 decrease in the signal required for the system to maintain height, [?].

584 4.4. Fast line - Transition mode

585 It presents a development of an experiment where the aircraft is tested on maximum velocity
 586 conditions on indoor. The line design is 5 meters on the same axis, and the initial condition is to

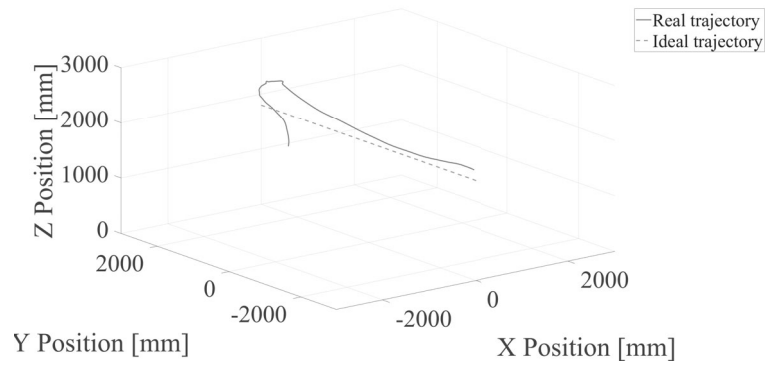


Figure 33. XYZ trajectory tracking, real vs ideal.

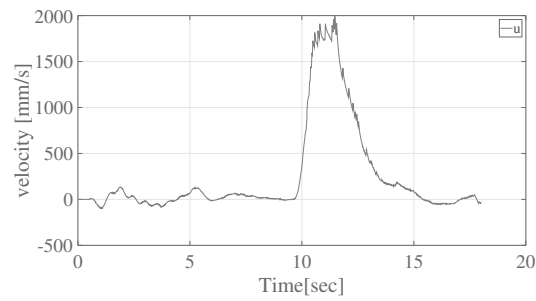


Figure 34. U velocity develop at Ramp

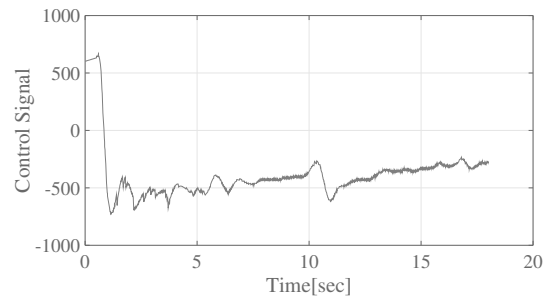


Figure 35. Lift behavior on global rotor forces

587 execute a hover flight, followed by a fast line, and end with an instant decrease of velocity on the
 588 system, see Figure 36.

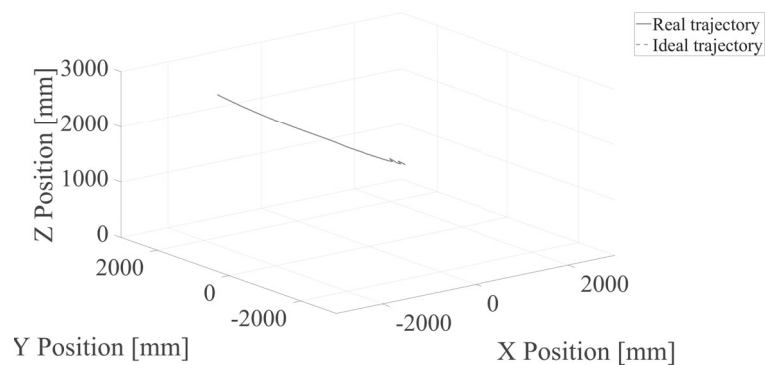


Figure 36. XYZ trajectory tracking, real vs ideal.

589 The vehicle followed the trajectory even under demanding conditions. Some errors are expected,
590 in this case, 300 mm on average; see Figure 37.

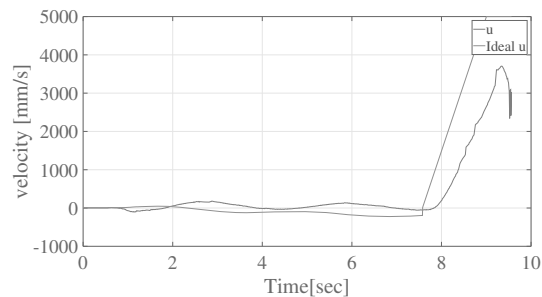


Figure 37. U velocity develop at line

591 Even the maximum condition on the system is required; just 3.7m/s is reached due to space
592 limitations.

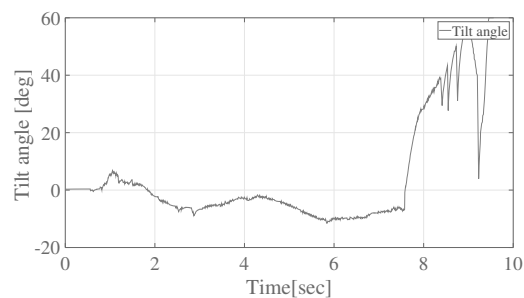


Figure 38. Servos transition phase

593 On a complete flight, the system is reached in the cruise phase, but in the transition phase, only
594 the change at 55 deg are reached by tilting rotors. In the transition phase, the vehicle reaches 90 deg on
595 a complete transition, as can be seen in Figure 38.

596 In the following link, a test video is shown: <https://youtu.be/h5RhDCh6QtQ?si=5Vn01xTrUZ-YuJhNIt>
597 is important to mention that a circle experiment was developed in this video.

598 5. Conclusions

599 The design of a convertible UAV platform capable of executing hover and cruise flight missions
600 was presented, having characteristics of a helicopter and an aircraft. The design was validated by
601 taking into account the structural refinement and airfoil-based design methodology; each stage
602 addressed critical aspects of design based on conceptual aerodynamics, mechanical properties, and
603 material selection. Additive manufacturing was used to develop the proposed vehicle, considering the
604 optimization techniques used to obtain a lightweight vehicle structure. The control strategy provided
605 an effective performance for hover and cruise flights of the convertible UAV, and it was designed to
606 ensure complete flight regimes. Notable achievements included reduced control authority reliance on
607 rotors and effective lift generation by the main wing during cruise flights. Validation experiments,
608 encompassing the convertible UAV approach, revealed promising results in trajectory tracking and
609 efficient flight maneuvers.

610
611 **Author Contributions:** Conceptualization, E.U.R.-R.; methodology, E.U.R.-R.; software, E.U.R.-R.
612 and E.G.R.-R.; validation, E.U.R.-R. and S.E.-A.; formal analysis, E.U.R.-R. and O.G.-S.; investigation,
613 S.E.-A. and O.G.-S.; resources, O.G.-S.; data curation, E.G.R.-R. and S.E.-A.; writing—original draft
614 preparation, E.U.R.-R.; writing—review and editing, E.U.R.-R. and S.E.-A.; visualization, E.G.R.-R. and
615 S.E.-A.; supervision, O.G.-S.; project administration, O.G.-S.; funding acquisition, O.G.-S. All authors

616 have read and agreed to the published version of the manuscript.

617

618 **Funding:** This research was supported by the Office of Naval Research Global through the grant
619 number N62909-20-1-2030.

620

621 **Institutional Review Board Statement:** Not applicable.

622

623 **Informed Consent Statement:** Not applicable.

624

625 **Data Availability Statement:** The data presented in this study are available on request from the
626 corresponding author.

627

628 **Acknowledgments:** The authors would like to thank the Aerospace Engineering Research
629 and Innovation Center of the Faculty of Mechanical and Electrical Engineering at the Autonomous
630 University of Nuevo Leon and the Department of Aeronautical and Astronautical Engineering at the
631 University of Southampton for the facilities of this research.

632

633 **Conflicts of Interest:** The authors declare no conflict of interest.

634

635 References

- 636 1. McCormick, B. *Aerodynamics of V/STOL flight*. 1967.
- 637 2. Semotiuk, L.; Józwiak, J.; Kukielka, K.; Dziedzic, K. Design and FEM Analysis of an Unmanned Aerial
638 Vehicle Wing. 2021 IEEE 8th International Workshop on Metrology for AeroSpace (MetroAeroSpace), 2021,
639 pp. 365–370.
- 640 3. Phung, D.K.; Morin, P. Modeling and Energy Evaluation of Small Convertible UAVs. *IFAC Proceedings*
641 *Volumes* **2013**, *46*, 212–219.
- 642 4. Greenwood, W.W.; Lynch, J.P.; Zekkos, D. Applications of UAVs in Civil Infrastructure. *Journal of*
643 *Infrastructure Systems* **2019**, *25*, 04019002,
- 644 5. Lozano, R. *Unmanned Aerial Vehicles Embedded Control*, 1 ed.; John Wiley-ISTE Ltd: USA, 2010.
- 645 6. Aláez, D.; Olaz, X.; Prieto, M.; Villadangos, J.; Astrain, J. VTOL UAV digital twin for take-off, hovering and
646 landing in different wind conditions. *Simulation Modelling Practice and Theory* **2023**, *123*, 102703.
- 647 7. Lu, K.; Liu, C.; Li, C.; Chen, R. Flight Dynamics Modeling and Dynamic Stability Analysis of Tilt-Rotor
648 Aircraft. *International Journal of Aerospace Engineering* **2019**, *2019*, 5737212.
- 649 8. Liu, N.; Wang, Y.; Zhao, J.; Cheng, X.; He, X.; Wu, K. A new inclining flight mode and oblique takeoff
650 technique for a tiltrotor aircraft. *Aerospace Science and Technology* **2023**, *139*, 108370.
- 651 9. Bautista, J.A.; Osorio, A.; Lozano, R. *Modeling and Analysis of a Tricopter/Flying-Wing Convertible UAV with*
652 *Tilt-Rotors*, 1 ed.; International Conference on Unmanned Aircraft Systems: Miami, FL, 2017.
- 653 10. Chamola, V.; Kotesch, P.; Agarwal, A.; Naren.; Gupta, N.; Guizani, M. A Comprehensive Review of
654 Unmanned Aerial Vehicle Attacks and Neutralization Techniques. *Ad Hoc Networks* **2021**, *111*, 102324.
- 655 11. Ducard, G.J.; Allenspach, M. Review of designs and flight control techniques of hybrid and convertible
656 VTOL UAVs. *Aerospace Science and Technology* **2021**, *118*, 107035.
- 657 12. Flores, G.; Escareno, J.; Lozano, R.; Salazar, S. Quad-Tilting Rotor Convertible MAV : Modeling and
658 Real-time Hover Flight Control. *Journal of Intelligent and Robotic Systems* **2012**, *65*, 457–471.
- 659 13. de Oliveira, T.L.; Anglade, A.; Hamel, T.; Samson, C. Control of convertible UAV with vectorized thrust.
660 *IFAC-PapersOnLine* **2023**, *56*, 9288–9293.
- 661 14. Bronz, M.; Smeur, E.J.; de Marina, H.G.; Hattenberger, G. Development of A Fixed-Wing mini UAV with
662 Transitioning Flight Capability. American Institute of Aeronautics and Astronautics, 2017.
- 663 15. Goh, G.; Agarwala, S.; Goh, G.; Dikshit, V.; Sing, S.; Yeong, W. Additive manufacturing in unmanned aerial
664 vehicles (UAVs): Challenges and potential. *Aerospace Science and Technology* **2017**, *63*, 140–151.

- 665 16. Moon, S.K.; Tan, Y.E.; Hwang, J.; Yoon, Y.J. Application of 3D printing technology for designing
666 light-weight unmanned aerial vehicle wing structures. *International Journal of Precision Engineering and*
667 *Manufacturing-Green Technology* **2014**, *1*, 223–228.
- 668 17. Yanguo, S.; Huanjin, W. Design of Flight Control System for a Small Unmanned Tilt Rotor Aircraft. *Chinese*
669 *Journal of Aeronautics* **2009**, *22*, 250–256.
- 670 18. Hassanalian, M.; Salazar, R.; Abdelkefi, A. Conceptual design and optimization of a tilt-rotor micro air
671 vehicle. *Chinese Journal of Aeronautics* **2019**, *32*, 369–381.
- 672 19. He, C.; Chen, G.; Sun, X.; Li, S.; Li, Y. Geometrically compatible integrated design method for conformal
673 rotor and nacelle of distributed propulsion tilt-wing UAV. *Chinese Journal of Aeronautics* **2023**, *36*, 229–245.
- 674 20. Sanchez, A.; Escareño, J.; Garcia, O.; Lozano, R. Autonomous Hovering of a Noncyclic Tiltrotor UAV:
675 Modeling, Control and Implementation. *IFAC Proceedings Volumes* **2008**, *41*, 803–808. 17th IFAC World
676 Congress.
- 677 21. D’Amato, E.; Di Francesco, G.; Notaro, I.; Tartaglione, G.; Mattei, M. Nonlinear Dynamic Inversion and
678 Neural Networks for a Tilt Tri-Rotor UAV. *IFAC-PapersOnLine* **2015**, *48*, 162–167. 1st IFAC Workshop on
679 Advanced Control and Navigation for Autonomous Aerospace Vehicles ACNAAV’15.
- 680 22. Campos, J.M.; Cardoso, D.N.; Raffo, G.V. Robust Adaptive Control with Reduced Conservatism for a
681 Convertible UAV. *IFAC-PapersOnLine* **2023**, *56*, 4520–4526. 22nd IFAC World Congress.
- 682 23. Bauersfeld, L.; Spannagl, L.; Ducard, G.J.J.; Onder, C.H. MPC Flight Control for a Tilt-Rotor VTOL Aircraft.
683 *IEEE Transactions on Aerospace and Electronic Systems* **2021**, *57*, 2395–2409.
- 684 24. Wang, H.; Sun, W.; Zhao, C.; Zhang, S.; Han, J. Dynamic Modeling and Control for Tilt-Rotor UAV Based
685 on 3D Flow Field Transient CFD. *Drones* **2022**, *6*.
- 686 25. Zhao, H.; Wang, B.; Shen, Y.; Zhang, Y.; Li, N.; Gao, Z. Development of Multimode Flight Transition
687 Strategy for Tilt-Rotor VTOL UAVs. *Drones* **2023**, *7*.
- 688 26. Fayez, K.; Leng, Y.; Jardin, T.; Bronz, M.; Moschetta, J.M. Conceptual Design for Long-Endurance
689 Convertible Unmanned Aerial System. American Institute of Aeronautics and Astronautics, 2021.
- 690 27. Carlson, S., A Hybrid Tricopter/Flying-Wing VTOL UAV. In *52nd Aerospace Sciences Meeting*.
- 691 28. Prach, A.; Kayacan, E. An MPC-based position controller for a tilt-rotor tricopter VTOL UAV. *Optimal*
692 *Control Applications and Methods* **2018**, *39*, 343–356.
- 693 29. Valavanis, K.; Vachtsevanos, G. *Handbook of Unmanned Aerial Vehicles*, 1 ed.; Springer: Atlanta, USA, 2015.
- 694 30. Rozvany, G. The SIMP method in topology optimization - Theoretical background, advantages and new
695 applications. 2000.
- 696 31. Telli, K.; Kraa, O.; Himeur, Y.; Ouamane, A.; Boumehraz, M.; Atalla, S.; Mansoor, W. A Comprehensive
697 Review of Recent Research Trends on Unmanned Aerial Vehicles (UAVs). *Systems* **2023**, *11*.
- 698 32. Stengel, R. *Flight Dynamics*, 1 ed.; Princeton University Press: USA, 2004.
- 699 33. Garcia Salazar, O.; Rojo Rodriguez, E.G.; Sanchez-Orta, A.; Saucedo Gonzalez, D.; Muñoz-Vázquez, A.
700 Robust Geometric Navigation of a Quadrotor UAV on SE(3). *Robotica* **2019**, *38*.
- 701 34. Ollervides-Vazquez, E.J.; Rojo-Rodriguez, E.G.; Rojo-Rodriguez, E.U.; Cabriales-Ramirez, L.E.;
702 Garcia-Salazar, O. Two-layer saturated PID controller for the trajectory tracking of a quadrotor UAV.
703 2020 International Conference on Mechatronics, Electronics and Automotive Engineering (ICMEAE), 2020,
704 pp. 85–91.
- 705 35. Garcia, O.; Sanchez, A.; Escareño, J.; Lozano, R. Tail-sitter UAV having one tilting rotor: Modeling, Control
706 and Real-Time Experiments. *IFAC Proceedings Volumes* **2008**, *41*, 809–814. 17th IFAC World Congress.